

# Quantum embedding study of strain and charge induced Stark effects on the NV<sup>-</sup> center in diamond

Gabriel I. López-Morales,<sup>1</sup> Joanna M. Zajac,<sup>2</sup> Johannes Flick,<sup>1,3,4</sup> Carlos A. Meriles,<sup>1,4</sup> and Cyrus E. Dreyer<sup>3,5</sup>

<sup>1</sup>*Department of Physics, City College of the City University of New York, New York, New York 10031, USA*

<sup>2</sup>*Instrumentation Division, Brookhaven National Laboratory,  
Bldg. 535 P.O. Box 5000, Upton, New York 11973-5000, USA*

<sup>3</sup>*Center for Computational Quantum Physics, Flatiron Institute,  
162 5th Avenue, New York, New York 10010, USA*

<sup>4</sup>*The Graduate Center of the City University of New York, New York, New York 10016, USA*

<sup>5</sup>*Department of Physics and Astronomy, Stony Brook University, Stony Brook, New York, 11794-3800, USA*

(Dated: June 13, 2024)

The NV<sup>-</sup> color center in diamond has been demonstrated as a powerful nanosensor for quantum metrology, due to the sensitivity of its optical and spin properties to external electric, magnetic, and strain fields. In view of these applications, we use quantum embedding to derive a many-body description of strain and charge induced Stark effects on the NV<sup>-</sup> center. We quantify how strain longitudinal to the axis of NV<sup>-</sup> shifts the excited states in energy, while strain with a component transverse to the NV axis splits the degeneracies of the <sup>3</sup>E and <sup>1</sup>E states. The largest effects are for the optically relevant <sup>3</sup>E manifold, which splits into  $E_x$  and  $E_y$  with transverse strain. From these responses we extract strain susceptibilities for the  $E_{x/y}$  states within the quasi-linear regime. Additionally, we study the many-body dipole matrix elements of the NV<sup>-</sup> and find a permanent dipole 1.64 D at zero strain, which is  $\sim 30\%$  smaller than that obtained from recent density functional theory calculations. We also determine the transition dipole between the  $E_x$  and  $E_y$  and how it evolves with strain.

## I. INTRODUCTION

The negatively-charged nitrogen vacancy (NV<sup>-</sup>) center in diamond is the most well-developed platform for realizing color-center based quantum and nanoscale technologies. As its name suggest, the NV<sup>-</sup> is formed through a combination of a carbon vacancy and an adjacent nitrogen substitution, with an excess electronic charge that typically comes from a nearby donor defect in the diamond lattice. Extensive experimental and theoretical work on its mechanisms of formation, charge-state stability and dynamics, as well as its interesting spin properties, has led to a well-founded understanding about the overall electronic structure of this color center in diamond [1–8].

In particular, nanoscale sensing constitutes an area of applications where the optoelectronic properties of the NV<sup>-</sup> have been exploited with great success [9–11]. High-precision temperature sensing, magnetometry-based bio-imaging, and noise spectroscopy at the nanoscale, are all recent applications based on optical and microwave manipulation of the excited states of the NV<sup>-</sup> center through its spin-selective transitions [11–15]. The NV<sup>-</sup> is also useful in sensing local electric fields at the nanoscale with high precision [16–22]. The lack of inversion symmetry in this color center facilitates the emergence of static electric dipoles for some of its electronic states [4, 23, 24], which interact with the external (e.g., local or applied) electric fields such that it results in spectral shifts of optical transitions. This phenomenon is broadly known as the electric Stark effect. The presence of local or macroscopically-applied strain fields has somewhat equivalent effects on the NV<sup>-</sup>; i.e., they intro-

duce strain-induced Stark shifts or splitting of the optical lines [4, 23–27]. Altogether, these Stark effects in the NV<sup>-</sup> could be further harnessed to implement novel NV-based spectroscopy and sensing protocols [25, 26, 28, 29], including for high-energy detectors [30–34]

For use of NV<sup>-</sup> as a nanosensor, it is crucial to have a quantitative understanding of the strain and electric field induced Stark shifts. The first experimental study to estimate the electric-field susceptibility (permanent dipole) of the NV<sup>-</sup>, provided 1.2–1.5 D [16]; more recently, this number was estimated to have longitudinal and transverse components of 2.82 and 3.63 D, respectively [21]. Studies employing the modern theory of polarization through density functional theory (DFT) have found a permanent dipole of 4.33 D [24], compared to 2.23–2.68 D obtained through direct computation of the electric-field Stark shift in the NV<sup>-</sup> through DFT [35]. An application of group theory, on the other hand, finds 0.79 D [23]. Other works employing few-level Hamiltonians and molecular-orbital approaches to treat the properties of the NV<sup>-</sup> under strain provided useful insights on the strain responses, but did not provide explicit numbers for the dipole couplings [1, 2]. Although some of these theoretical results are relatively close to experimental observations and provide valuable information about Stark effects on the NV<sup>-</sup>, further work is required to fully quantify its dipole couplings and understand the physics underlying the evolution of the optical excited states of this color center under minute external (e.g., strain, electric) fields.

In particular, this defect center features a non-negligible degree of electronic correlations within its set of  $sp^3$ -hybridized localized electrons, two of which are

unpaired. It has become increasingly evident that an adequate treatment of such correlations is required to quantitatively describe the excited-state properties of the NV<sup>-</sup> [36–40]. In these regards, a full *ab-initio* description of the many-body physics of this defect center, most of which is central for applications such as nanoscale sensing, is highly desirable and constitutes an area of ongoing research efforts [36–42]. Recent work employing methods that combine quantum chemistry and density functional theory (DFT) via quantum embedding have demonstrated quantitative descriptions of the NV<sup>-</sup> excited states, at convenient computational costs [36, 37, 39, 42]. Thus, developing a quantitative description of strain- and charge induced Stark effects on the optical transitions of the NV<sup>-</sup> through such methods has important implications for NV-based nanoscale sensors.

In this paper, we a first-principles approach based on quantum embedding to derive such a description. We study the NV<sup>-</sup> under strain to derive a many-body description of strain susceptibilities in its optical excited states. We also access the many-body dipole moments of the NV<sup>-</sup> center and strain induced effects in the optical transitions of the NV center by considering many-body transition dipoles between excited states.

The paper is organized as follows. In Sec. II we discuss the computational methodology employed in this work and the computational details. Then, we present the obtained results for strain susceptibilities and dipole couplings in Secs. III A and III B. This is followed by a discussion of the results in Sec. IV, and the conclusions in Sec. V.

## II. COMPUTATIONAL METHODOLOGY

### A. DFT for structure and strain

As a basis for the quantum embedding, we employ DFT calculations to obtain the relaxed atomic structure and the corresponding electronic ground state of a diamond supercell containing a single NV<sup>-</sup> center, with axis along the  $\langle 1, 1, 1 \rangle$ . Calculations are performed using the 216-atom ( $3 \times 3 \times 3$ ) diamond supercell, which is found to yield converged many-body states within our methodology [39]. To study the evolution of the electronic states of the NV<sup>-</sup> under strain, we introduce distortions to the supercell via direct elongation (contraction) of the lattice vectors for tensile (compressive) strain. For simplicity, we focus on two cases of strain: (i) along the  $\langle 1, 1, 1 \rangle$  axis ( $\varepsilon_{\langle 1, 1, 1 \rangle}$ ), (ii) along the  $\langle 1, -1, 1 \rangle$  axis ( $\varepsilon_{\langle 1, -1, 1 \rangle}$ ). These two directions of strain fields are also experimentally relevant because the NV<sup>-</sup> is known to respond differently under longitudinal and transverse strains [2, 3, 23, 24]. The amount of strain applied on each component of the lattice vectors is taken as  $|\varepsilon|$ , and defined with respect to the length of the pristine lattice vectors.

### B. Quantum embedding

From the ground-state DFT calculation of NV<sup>-</sup>, we downfold onto a minimal active space containing only the defect states of NV<sup>-</sup> via Wannierization (using the Wannier90 code) [43]. The down-folded problem is mapped onto the effective Hamiltonian [36, 37, 39]

$$\begin{aligned} \hat{H}_{\text{eff}} = & - \sum_{\langle ij \rangle, \sigma} (t_{ij} c_{i\sigma}^\dagger c_{j\sigma} + h.c.) \\ & + \frac{1}{2} \sum_{\langle ijkl \rangle, \sigma, \sigma'} U_{ijkl} c_{i\sigma}^\dagger c_{j\sigma'}^\dagger c_{l\sigma'} c_{k\sigma} \\ & - \hat{H}_{DC}, \end{aligned} \quad (1)$$

where  $c^\dagger$  ( $c$ ) represent creation (annihilation) operators, and  $i, j, k, l$  label different correlated defect states within the active space, with spin  $\sigma, \sigma'$ . The first term in Eq. (1) represents the single-particle part of the effective Hamiltonian and is characterized by the hopping matrix elements  $t_{ij}$  in the Wannier basis. The hopping matrix elements are determined from the Wannierized basis functions  $\psi$  as

$$t_{ij} = - \langle \psi_i | \hat{H}_{\text{KS}} | \psi_j \rangle. \quad (2)$$

In the absence of disentanglement from bulk bands, the eigenvalues of  $t_{ij}$  reproduce the KS eigenvalues exactly [44]. The second term in Eq. (1) captures the effective electron-electron interactions between correlated states within the active space, in this case represented via the four-body screened Coulomb tensor  $U_{ijkl}$ . We calculate these effective interactions using the constrained random-phase approximation (cRPA) [45], via

$$U_{ijkl} = \langle \psi_i \psi_j | \hat{U} | \psi_k \psi_l \rangle. \quad (3)$$

To do so, we evaluate a decomposed version of the full polarizability tensor  $\hat{\Pi}_{\text{full}}$  containing all screening effects except those among states within the correlated subspace

$$\hat{U} = [1 - \hat{V}(\hat{\Pi}_{\text{full}} - \hat{\Pi}_{\text{NV}})] \hat{V}. \quad (4)$$

Here, “NV” refers to the correlated subspace comprised of the defect states associated with the NV<sup>-</sup> center, and  $\hat{V}$  is the bare Coulomb interaction. In this way, the correlated defect manifold described by Eq. (1) couples to the diamond matrix through the screening effects included while evaluating the Coulomb tensor. Screening effects and correlations within the active space of the defect are included explicitly through the configuration interaction (CI) by diagonalization Eq. (1) exactly (using the triqs software library [46]). The last term in Eq. (1), so-called double-counting (DC) correction, is added to deal with unwanted Coulomb interactions partially included (from DFT) in the single-particle parts of the full effective Hamiltonian. Here, we adopt a DC correction of the form [36, 37, 39]

$$\hat{H}_{DC} = \sum_{\langle ij \rangle, \sigma} c_{i\sigma}^\dagger c_{j\sigma} \sum_{\langle kl \rangle} P_{kl} (U_{iljk} - \alpha U_{ilkj}), \quad (5)$$

where, following Ref. [36],  $\alpha$  relates to the amount of Hartree-Fock exchange mixed to construct the DFT functional. Since we use the Heyd-Scuseria-Ernzerhof (HSE) hybrid functional in all DFT calculations, we set  $\alpha = 0.25$ . Employing this DC scheme has shown to yield  $NV^-$  excitation energies in good agreement with those from experiments [36, 39]. In any case, the quantities of interest in this work and their trends with strain are quantitatively very similar to those obtained without DC corrections.

### C. Many-body dipole couplings

To describe the dipole couplings to electric fields of the  $NV^-$ , we evaluate the dipole matrix elements across the many-body spectrum via

$$\boldsymbol{\mu}_{ij} = \langle \Psi_i | \hat{\mathbf{r}} | \Psi_j \rangle, \quad (6)$$

where,  $\Psi$  denotes many-body wave functions of states  $i$  and  $j$  (respectively), and  $\hat{\mathbf{r}}$  represents the many-body dipole operator (along the Cartesian directions). In our formalism, we construct the many-body dipole operator as

$$\hat{\mathbf{r}} = \sum_{nm} \mathbf{r}_{nm}^{\text{wann}}(\mathbf{0}) c_n^\dagger c_m, \quad (7)$$

using the matrix elements of the position operator between Wannier functions  $m$  and  $n$ , given by

$$\mathbf{r}_{nm}^{\text{wan}}(\mathbf{R}) = \langle n\mathbf{0} | \mathbf{r} | m\mathbf{R} \rangle, \quad (8)$$

as implemented in Wannier90 [43]. This approach allows for permanent and transition dipole matrix elements between explicitly *many-body* ground and excited states of  $NV^-$ . We note that some properties of the dipole matrix elements might depend on the specific gauge chosen for constructing out Wannier functions. To quantify this, we evaluated the dipole matrix (in the absence of strain) using a Wannierization procedure slightly different from that employed for the main results (Sec. II D), i.e., increasing the disentanglement window slightly, but other properties of our many-body model (i.e., energies, spin state, symmetries) are not significantly altered. We make use of these results to comment on possible uncertainties regarding the absolute orientation for some of the dipoles in the  $NV^-$  (see Sec. III B).

### D. Wannierization

In terms of the Wannierization scheme specifically implemented for the  $NV^-$  defect center, we rely on initial projections of  $sp^3$ -hybrid Wannier functions centered around the NV to obtain the localized atomic basis orbitals. This basis is utilized to evaluate the screened Coulomb interactions and subsequently perform

all cRPA-CI calculations. The single-particle electronic states relevant for most of the optical excitations of the  $NV^-$  center are the  $a_1(1)$ ,  $a_1(2)$ ,  $e_x$ , and  $e_y$ . While the  $a_1(2)$ ,  $e_x$ , and  $e_y$  lie isolated within the bandgap, the  $a_1(1)$  state is resonant with the valence band (VB) of diamond, requiring disentanglement during the Wannierization procedure. Hence, we set our disentanglement window to include the  $a_1(1)$  state, while the  $a_1(2)$ ,  $e_x$  and  $e_y$  states are kept “frozen” such that Eq. (2) reproduces the DFT eigenvalues exactly. All Wannierized states are maximally-localized by minimizing the Wannier spreads. Overall, our active space is comprised of the four  $a_1(1)$ ,  $a_1(2)$ ,  $e_x$ , and  $e_y$  Wannierized orbitals and 6 electrons. This active space has demonstrated to be sufficient to yield quantitative agreement between calculated and experimental excitation energies for the  $NV^-$  [36, 39]. The main task concerning our current work centers on studying how this active space and its many-body states evolve under the external influence of strain, as we discuss in Sec. III.

## III. RESULTS

### A. Strain susceptibilities of $NV^-$

We start by considering the case of strain along the  $\langle 1, 1, 1 \rangle$ . Since this strain propagates along the high-symmetry axis of the  $NV^-$  center ( $A_1$  strain), the  $C_{3v}$ -symmetry of the defect is preserved. As a result, the  ${}^3E$  states remain degenerate, but shift in energy with respect to the  ${}^2A_2$  ground state as a function of  $\varepsilon_{\langle 1, 1, 1 \rangle}$  [Fig. 1(a)]. The lack of inversion symmetry in the NV center is reflected in the asymmetric evolution of the excited states under  $\pm \varepsilon$  (elongation or compression). Overall, these results indicate that in the scenario where local strain is only longitudinal to the NV axis, a red-shift in the optical transition of the  $NV^-$  corresponds to local compressive strain, while tensile strain will manifest as a blue shift in the optical transition. Lastly, Fig. 1(a) clearly illustrates that the energy shifts are much larger for the  ${}^3E$  manifold compared to the singlet excited states, confirming that the triplet manifold is much more sensitive to longitudinal strain.

Under  $\varepsilon_{\langle 1, -1, 1 \rangle}$ , the picture is more complicated. Here, the strain has both longitudinal and transverse components to the local  $NV^-$  axis. The  $C_{3v}$  symmetry is thus broken and the degeneracy of the  $E$  states is lifted [Fig. 1(b)]. The evolution of the excited states under  $\varepsilon_{\langle 1, -1, 1 \rangle}$  still includes energy shifts caused by the longitudinal strain components. Again, the  ${}^3E$  states show the largest strain induced effects. However, in this case the  ${}^1E$  states also display a relatively strong response. This splitting correlates well with observations of split optically-detected magnetic resonance through the singlet transition [47, 48]. In a sense, the singlet manifold could be an interesting probe for strain sensing under specific conditions, e.g., in the near-infrared spec-

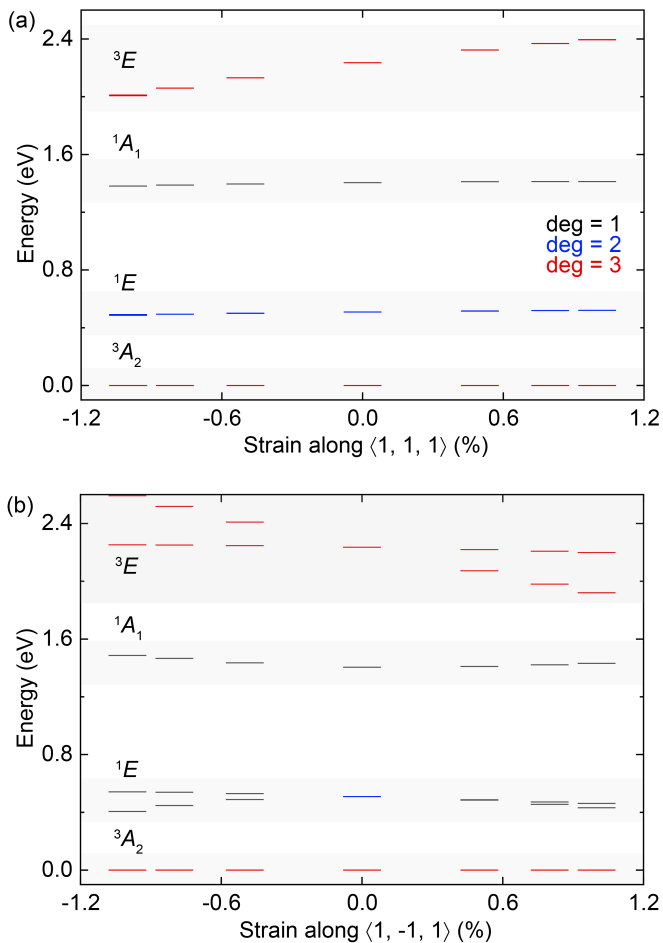


FIG. 1. Many-body spectrum of the  $\text{NV}^-$  center in the presence of strain. (a)  $\varepsilon_{\langle 1, 1, 1 \rangle}$  introduces energy shifts of the  ${}^3E$  manifold with respect to the  ${}^3A_2$  ground state. Energy shifts of the other manifolds are comparatively much smaller. (b)  $\varepsilon_{\langle 1, -1, 1 \rangle}$  introduces an energy split of the  ${}^3E$  into the  ${}^3E_{x/y}$  sub-manifolds. The  ${}^1E$  manifold also splits under such strain, while the  ${}^1A_1$  state shows larger shifts compared to the  $\langle 1, 1, 1 \rangle$ -strained case.

tral region, given its weak/strong response to longitudinal/transverse strains [Figs. 1(a) and 1(b)]. However, the inter-system crossing required for populating the singlet manifold is typically a slow process, which, combined with a smaller radiative efficiency and longer decay lifetime [47, 48], makes the photon collection in the singlet manifold poorer compared to the triplet optical transitions. With this in mind, we make the  ${}^3E$  manifold the focus of the remainder of this paper.

In Fig. 2, we make use of the strain evolution of the  ${}^3E$  states to extract the strain susceptibility (denoted here as  $\chi$ ) of the optical transitions in the NV center. As mentioned previously,  $\varepsilon_{\langle 1, 1, 1 \rangle}$  does not split the  ${}^3E$  manifolds. In this case,  $\chi$  is identical for the  ${}^3E_{y/x}$  states [Fig. 2(a)], and is found to follow an almost-linear response, with linear coefficient  $\chi_L = 19.2$  eV. The wide range of strain considered here allows to also capture the

quadratic component of the strain susceptibility  $\chi_Q$ , although the realistic range of strain (typically  $< 10^{-5}$ ) renders this contribution negligible within linear-strain regimes most relevant for experiments. In the case of  $\varepsilon_{\langle 1, -1, 1 \rangle}$ , the resulting quadratic susceptibility over the same range of strain is more pronounced [left panel of Fig. 2(b)], due to splitting of the  ${}^3E$  manifold.

The magnitude of strain fields experienced by  $\text{NV}^-$  centers in typical experiments is well below the strains considered up to this point, usually below  $\varepsilon = \pm 10^{-5}$  [18, 21, 22, 27, 28, 49–51]. Again, within this range of strain, the responses to  $\varepsilon_{\langle 1, 1, 1 \rangle}$  for the  ${}^3E_{y/x}$  states are effectively linear. Thus, to quantify  $\chi_L$  more reliably for transverse strain, we expand the resolution by considering a narrower range of strains around zero ( $\varepsilon < 10^{-4}$ ) for  $\varepsilon_{\langle 1, -1, 1 \rangle}$  [highlighted region in the left panel of Fig. 2(b)]. The obtained results for these calculations is presented in the right panel of Fig. 2(b). The fit to the numerical data obtained in this case is also improved by exclusion of the extreme points  $\varepsilon > 1.0\%$ , which are in any case well outside any realistic experimental situation. Compared to the left panel in Fig. 2(b), the set of points around zero-strain resemble a clearer linear response and the  $\chi_L$  extracted from this fit should be closer to that expected for calculations in the linear regime of strain.

Ideally, one would want to consider even weaker strain, such that the calculated strain evolution of the  ${}^3E_{y/x}$  states is explicitly matched to that obtained experimentally. However, such strain fields require very small atomic displacements, as well as the resolution of correspondingly small energy splittings of the single-particle/many-body states which are close to the numerical precision of our methods.

## B. Dipole couplings of $\text{NV}^-$ under strain

Within our methodology, we can obtain a many-body description of the permanent dipole and transition dipole moments (TDMs) of the  $\text{NV}^-$ , as well as possible strain induced effects on these dipole couplings. The diagonal elements of the full dipole matrix described in Sec. II C [Eq. (6)] are used to extract the permanent dipoles,  $\mathbf{p}_i \equiv \boldsymbol{\mu}_{ii}$ . To quantify the true permanent dipole character of the excited states of the  $\text{NV}^-$ , we take the many-body ground-state position as reference [24], i.e.,  $\Delta\mathbf{p}_{y/x} \equiv \langle {}^3E_{y/x} | \hat{\mathbf{r}} | {}^3E_{y/x} \rangle - \langle {}^3A_2 | \hat{\mathbf{r}} | {}^3A_2 \rangle$  for transitions to individual  ${}^3E$  states and  $\Delta\mathbf{p}_{\text{avg}} \equiv \langle {}^3E | \hat{\mathbf{r}} | {}^3E \rangle - \langle {}^3A_2 | \hat{\mathbf{r}} | {}^3A_2 \rangle$  for the average. A summary of these results is provided in Table I. First, the individual permanent dipoles for the  ${}^3E_{y/x}$  states are found to be tilted with respect to the local axis of the  $\text{NV}^-$  (here the  $\langle 1, 1, 1 \rangle$  axis, which we will refer to as  $\text{NV}_z^-$ ); the  $x$  and  $y$  components of  $\Delta\mathbf{p}_y$  and  $\Delta\mathbf{p}_x$  are anti-parallel (i.e., point in opposite directions) with respect to  $\text{NV}_z^-$ , while the  $z$  components of  $\Delta\mathbf{p}_y$  and  $\Delta\mathbf{p}_x$  are parallel and aligned along the  $\text{NV}_z^-$  axis. The net  $|\Delta\mathbf{p}_{\text{avg}}|$  (averaged between  ${}^3E_x$  and  ${}^3E_y$ ) is thus fully



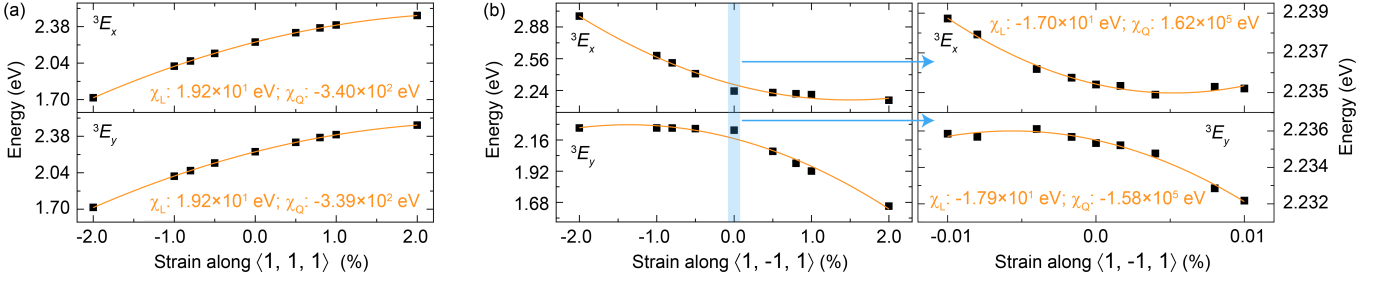


FIG. 2. Strain susceptibility ( $\chi$ ) for the  ${}^3E$  many-body states of the  $\text{NV}^-$  center. (a)  ${}^3E_{y/x}$  under  $\varepsilon_{\langle 1,1,1 \rangle}$ , covering a wide range of strain. (b) Left panel: Same as in (a), but for the case of  $\varepsilon_{\langle 1,-1,1 \rangle}$ . A set of higher-resolution calculations for this case of strain (within shaded region) is included in the right panel of (b), to better resolve the response within the strain region most relevant to experiments ( $\varepsilon < 10^{-5}$ ). The scatter and solid lines represent numerical data and second-degree polynomial fits, respectively.

TABLE I. Summarized dipole couplings for the  $\text{NV}^-$  under strain. The format of the dipole couplings presented below is “ $\Delta p_x, \Delta p_y, \Delta p_z, |\Delta \mathbf{p}|$ ” (or  $\Delta \mu_x, \Delta \mu_y, \Delta \mu_z, |\Delta \boldsymbol{\mu}|$  for the transition dipole moment in the last column). The “ $x, y, z$ ” represent directions along the supercell lattice vectors. In all cases, the applied strain is along the  $\langle 1, -1, 1 \rangle$  direction (negative values correspond to compressive strain).

$\varepsilon$ (%)	$\langle {}^3E_y   \hat{\mathbf{r}}   {}^3E_y \rangle - \langle {}^3A_2   \hat{\mathbf{r}}   {}^3A_2 \rangle$	$\langle {}^3E_x   \hat{\mathbf{r}}   {}^3E_x \rangle - \langle {}^3A_2   \hat{\mathbf{r}}   {}^3A_2 \rangle$	$\langle {}^3E   \hat{\mathbf{r}}   {}^3E \rangle - \langle {}^3A_2   \hat{\mathbf{r}}   {}^3A_2 \rangle$	$\langle {}^3E_y   \hat{\mathbf{r}}   {}^3E_x \rangle$
-0.008	0.054, 2.7, 0.075, 2.7	1.8, -0.82, 1.8, 2.7	0.94, 0.94, 0.94, 1.6	1.5, 0.016, 1.5, 2.2
-0.004	1.5, -0.73, 2.1, 2.7	0.42, 2.6, -0.21, 2.7	0.94, 0.94, 0.94, 1.6	1.7, 0.55, 1.3, 2.2
0.00	1.7, 1.7, -0.55, 2.4	0.19, 0.21, 2.4, 2.4	0.94, 0.94, 0.94, 1.6	1.6, 1.6, 0.94, 2.4
+0.004	1.6, -0.80, 2.0, 2.7	0.27, 2.7, -0.12, 2.7	0.94, 0.94, 0.94, 1.6	1.6, 0.27, 1.4, 2.2
+0.008	1.8, -0.82, 1.8, 2.7	0.072, 2.7, 0.051, 2.7	0.94, 0.94, 0.94, 1.6	1.5, 0.023, 1.5, 2.2

aligned with the local  $\text{NV}_z^-$  (see “ $\langle {}^3E | \hat{\mathbf{r}} | {}^3E \rangle - \langle {}^3A_2 | \hat{\mathbf{r}} | {}^3A_2 \rangle$ ” column in Table I). In the absence of strain, the individual permanent dipoles have magnitude of  $|\Delta \mathbf{p}_{y/x}| = 2.4$  D, while  $|\Delta \mathbf{p}_{\text{avg}}| = 1.6$  D. As a result, if one considers the unresolved  ${}^3A_2 \leftrightarrow {}^3E$  optical transition, i.e., via off-resonant excitation and/or at room temperature, the net dipole is effectively weaker. Furthermore, since the off-axis projections of  $|\Delta \mathbf{p}|$  are lost for the unresolved excited manifold, the possible sense of directionality from electric fields experienced by the  $\text{NV}^-$  should be substantially suppressed under such conditions. Overall, this would translate into an enhanced electric-field sensitivity when addressing the individual  ${}^3A_2 \leftrightarrow {}^3E_{y/x}$  transitions (resonantly), which correlates very well with experimental observations [16, 17, 19–22]. From our results, the “resonant enhancement” of  $|\Delta \mathbf{p}|$  is  $\sim 1.5$ .

Of course, other effects, such as phonon scattering and local strain environment, will likely impact the effective enhancement of the  $|\Delta \mathbf{p}|$  in resonant experiments. In fact, by considering strain effects explicitly, we find that  $|\Delta \mathbf{p}_{y/x}|$  increases for  $\varepsilon_{\langle 1,-1,1 \rangle}$ , but decreases with  $\varepsilon_{\langle 1,1,1 \rangle}$  (not shown). Naturally, the amount of enhancement/suppression of the permanent dipole depends on the magnitude of local applied strain, but from the results in Table I, it corresponds to  $< 12.5\%$  for  $|\varepsilon| \leq 0.008\%$ . Since  $\varepsilon_{\langle 1,-1,1 \rangle}$  is not fully perpendicular to the local  $\text{NV}_z^-$

axis, and introduces a transverse strain component, these results suggest that  $\varepsilon \perp \text{NV}_z^-$  could slightly enhance  $\Delta \mathbf{p}_{y/x}$  [52]. Additionally, the average permanent dipole remains constant with strain, which means that the relative enhancement of the  $\Delta \mathbf{p}_y$  components with strain is anti-correlated with that of  $\Delta \mathbf{p}_x$ , and if at all present, will only be quantifiable via resonant-excitation experiments. In terms of directionality, the obtained results show that while the individual dipoles change directions with  $\varepsilon_{\langle 1,-1,1 \rangle}$ , they always maintain anti-parallel alignment of their off-axis component, such that  $\Delta \mathbf{p}_{\text{avg}}$  is always along the  $\langle 1, 1, 1 \rangle$  (Table I). It is worth noting that the  $|\Delta \mathbf{p}_{\text{avg}}|$  magnitudes obtained herein are in excellent agreement with experimental estimations [16, 21] (similar to that for the  $\text{NV}^0$  [53]), also falling close to those derived through DFT [24, 35].

Since strain splits otherwise degenerate  ${}^3E_{y/x}$  states, one other dipole coupling of potential interest for strain sensing with the  $\text{NV}^-$  is the TDM between these states (denoted here  $\boldsymbol{\mu}_{y/x}$ ), represented by the off-diagonal elements of the full many-body dipole matrix. In the last column of Table I, we present such TDMs and how they evolve with strain. First, we see that in the  $\varepsilon = 0$  case this TDM has the same magnitude as the permanent dipole of the individual  ${}^3E_{y/x}$  states. This TDM is also comparable to that of the optical transition ( ${}^3A_2 \leftrightarrow {}^3E$ ), which we find to be  $\sim 2.7$  D (in the absence of strain). Of

course  $\boldsymbol{\mu}_{y/x}$  does not have much physical relevance here since with no strain to break the  $C_{3v}$  symmetry,  ${}^3E_x$  and  ${}^3E_y$  are degenerate to there will be no optical transitions.

Under the influence of strain,  $|\boldsymbol{\mu}_{y/x}|$  shows the opposite trend compared to the permanent dipoles, i.e.,  $|\boldsymbol{\mu}_{y/x}|$  is suppressed by  $\varepsilon_{\langle 1,-1,1 \rangle}$  and enhanced by  $\varepsilon_{\langle 1,1,1 \rangle}$  (results for the latter case are not shown for brevity). The maximum change in  $|\boldsymbol{\mu}_{y/x}|$  for the strain range considered herein is  $\sim 8\%$ . Interestingly, the direction of  $\boldsymbol{\mu}_{y/x}$  is initially ( $\varepsilon = 0$ ) almost fully aligned with the  $\langle 1, 1, 1 \rangle$  (with  $\sim 5$ -deg misalignment); under strain, one component of the TDM is significantly suppressed. Though we caution that the details of the dipole direction may be effected by the gauge choice for our Wannier functions (see Sec. IV for more discussion), this corresponds to the expected behavior from the symmetry of the system. The transverse strain breaks the  $C_3$  rotation symmetry of  $NV^-$ , but keeps one mirror plane. Under the new  $C_s$  point group, states with  $E$  symmetry split into  $A'$  and  $A''$ . Based on the selection rules for optical transitions under this symmetry, we expect the TDM perpendicular to the mirror plane to be suppressed, which is approximately the  $y$  direction in Table I.

These last set of results hint at the  ${}^3E_y \leftrightarrow {}^3E_x$  transition as an alternative candidate for strain sensing using the  $NV^-$ . For instance, provided there is enough strain to split the  ${}^3E_{y/x}$  states (which is true for the majority of NV centers in real experiments), the response in  $|\boldsymbol{\mu}_{y/x}|$  coupling with transverse and longitudinal strain (opposite to that of  $\Delta\mathbf{p}_{y/x}$ ) could help identify how much of each component is locally contributing to the overall strain experienced by the  $NV^-$ . Since typical  ${}^3E_{y/x}$  splitting is on the order of few GHz, the relatively large  $\boldsymbol{\mu}_{y/x}$  should make it straightforward to sense strain by monitoring the amplitude of this transition under resonant excitation. Additionally, since this transition appears almost fully linearly polarized, and its directionality reacts to the direction of the overall strain, it could help decompose the local strain in its vector components. Lastly, the measurements required to probe  $|\boldsymbol{\mu}_{y/x}|$  are, in principle, independent from those required to monitor the Stark shifts on the ZPL through the permanent dipole. Thus, combining information from these two complementary dipole couplings should provide an enhanced probe for strain sensing using the  $NV^-$  center.

#### IV. DISCUSSION

The results described in Sec. III provide useful insights on the intricate response of the  $NV^-$  to local strain and electric fields. For instance, the asymmetric evolution of the excited states with strain appears to be more prominent when the strain has both transverse and parallel components to the  $NV_z$  axis. This behavior, emerging from the absence of inversion symmetry on the NV centre, should provide a means of differentiating local compressive versus tensile strains. On the

other hand, from the relative energy shifts and splitting under  $\varepsilon_{\langle 1,1,1 \rangle}$  and  $\varepsilon_{\langle 1,-1,1 \rangle}$  shown in Fig. 1, one could argue that the singlet transition is more reliable at differentiating transverse versus longitudinal strains than the triplet transition. This could be an interesting application of the singlet transitions in the  $NV^-$  for local strain sensing: the triplet manifold reacts to both longitudinal and transverse strains (via shifts and splitting of the optical line, respectively), while the singlet reacts (splits) most prominently only to transverse components of strain. In essence, correlated high-resolution measurements in which both the triplet and singlet transitions are interrogated through resonant excitations should provide useful information about strain propagation through diamond at the nanoscale. Further, given the increasing interest in studying closely-positioned  $NV^-$  centers in diamond [21, 22, 52, 54], these proposed measurements could serve as useful probes for possible  $NV^-$ - $NV^-$  interactions mediated via strain.

Another interesting aspect of the results in Sec. III is the non-negligible susceptibility of some of the dipole couplings in the  $NV^-$  to local strain. For example, since the permanent dipoles dictate how the optical transitions of the  $NV^-$  couple to local electric fields, strain emerges as a natural means for potentially enhancing its electric-field sensitivity. Furthermore, the magnitude of the transition dipoles between  ${}^3E_{y/x}$  states also appear slightly susceptible to local strain, with a seemingly strong change in the individual components (polarization). However, as mentioned in Sec. II C, these TDMs are likely to have a degree of gauge-dependence within our methodology, resulting in possible uncertainties in their absolute orientations. We can estimate such uncertainties by changing slightly the choice of Wannier functions that construct our basis. For instance, increasing the disentanglement window by 350 meV (in the absence of strain), we find that the net permanent dipole remains almost unchanged in both direction and magnitude (fully gauge-invariant). Its individual components ( $\Delta\mathbf{p}_{y/x}$ ) maintain the same angle with respect to the  $NV_z^-$  axis, with an increase of only  $\sim 6$  deg in the angle between their Cartesian  $x$  and  $y$  components. It should be noted that these slight changes might be somewhat convoluted, since there could be a basis dependence for the  $\Delta\mathbf{p}_{y/x}$  since the  ${}^3E$  states are degenerate in the absence of strain, (full  $C_{3v}$  symmetry). Regarding the optical TDM ( ${}^3A_2 \leftrightarrow {}^3E$ ), the changes in its Cartesian components amount to a tilt of  $\sim 3$  deg between the two Wannier bases, while its magnitude changes by  $< 2\%$ . Lastly, the quantity that seems to vary the most from a slight change in the Wannier basis is the  $\boldsymbol{\mu}_{y/x}$ , with changes in its Cartesian components that amount to a tilt of  $\sim 15$  deg with respect to the  $\boldsymbol{\mu}_{y/x}$  from the main results (maximally-localized Wannier functions). Its magnitude changes by  $< 7\%$ . In all cases, the individual angles between each dipole vector and the local  $NV_z^-$  axis change by  $\leq 3$  deg between the two bases. While these differences in the individual components of the dipole vectors

translate into possible gauge-dependence of their absolute orientation, the key figures of merit for the sensing applications proposed herein (strength of permanent dipoles) are qualitatively unchanged. A more exhaustive study of these TDMs under strain is required to derive their relative orientations with full certainty. But, given that the current uncertainties are within experimental margins, we consider this a matter for future work.

## V. CONCLUSIONS

We have employed first-principles calculations based on density-functional theory and quantum embedding to derive a many-body description of strain and charge induced Stark effects in the  $NV^-$  defect center in diamond. The relaxed atomic structures of a diamond supercell containing a single  $NV^-$  under the influence of strain have been obtained from DFT. Using these as starting points for embedding calculations, we extract the strain susceptibility of the many-body states comprising the  ${}^3E$

excited-state manifold, as well as permanent and transition dipoles under strain. The results derived in this work are in excellent agreement with recent experiments, where the dipole couplings of the  $NV^-$  are estimated and/or used for sensing applications [16, 21, 22, 27, 52]. This work thus broadens our fundamental understanding on the optoelectronic properties of the  $NV^-$  center, and also highlights the utility of including many-body effects to describe the properties of defect-related color centres in solids for sensing applications.

## ACKNOWLEDGMENTS

CED acknowledges support from the National Science Foundation under Grant No. DMR-2237674. GILM acknowledges funding from grant NSF-2208863. JZ and CED acknowledge support from a joint SBU-BNL seed grant. The Flatiron Institute is a division of the Simons Foundation.

- 
- [1] L. J. Rogers, R. L. McMurtrie, M. J. Sellars, and N. B. Manson, Time-averaging within the excited state of the nitrogen-vacancy centre in diamond, *New J. Phys.* **11** (2009).
  - [2] M. W. Doherty, N. B. Manson, P. Delaney, and L. C. L. Hollenberg, The negatively charged nitrogen-vacancy centre in diamond: the electronic solution, *New J. Phys.* **13** (2011).
  - [3] M. W. Doherty, F. Dolde, H. Fedder, F. Jelezko, J. Wrachtrup, N. B. Manson, and L. C. L. Hollenberg, Theory of the ground-state spin of the  $NV^-$  center in diamond, *Phys. Rev. B* **85** (2012).
  - [4] M. W. Doherty, N. B. Manson, P. Delaney, F. Jelezko, J. Wrachtrup, and L. C. L. Hollenberg, The nitrogen-vacancy colour centre in diamond, *Physics Reports* **528**, 1 (2013).
  - [5] P. Deák, B. Aradi, M. Kaviani, T. Frauenheim, and A. Gali, Formation of NV centers in diamond: A theoretical study based on calculated transitions and migration of nitrogen and vacancy related defects, *Phys. Rev. B* **89**, 075203 (2014).
  - [6] G. Thiering and A. Gali, Theory of the optical spin-polarization loop of the nitrogen-vacancy center in diamond, *Phys. Rev. B* **98**, 085207 (2018).
  - [7] N. B. Manson, M. Hedges, M. S. J. Barson, R. Ahlefeldt, M. W. Doherty, H. Abe, T. Ohshima, and M. J. Sellars,  $NV^-$ - $N^+$  pair centre in 1b diamond, *New J. Phys.* **20**, 113037 (2018).
  - [8] L. Razinkovas, M. W. Doherty, N. B. Manson, C. G. V. de Walle, and A. Alkauskas, Vibrational and vibronic structure of isolated point defects: The nitrogen-vacancy center in diamond, *Phys. Rev. B* **104**, 045303 (2021).
  - [9] R. Schirhagl, K. Chang, M. Loretz, and C. L. Degen, Nitrogen-vacancy centers in diamond: Nanoscale sensors for physics and biology, *Nano Lett.* **65**, 83 (2014).
  - [10] G. Balasubramanian, A. Lazarev, S. R. Arumugam, and D. wen Duan, Nitrogen-vacancy color center in diamond - emerging nanoscale applications in bioimaging and biosensing, *Current Opinion in Chemical Biology* **20**, 69 (2014).
  - [11] T. Zhang, G. Pramanik, K. Zhang, M. Gulka, L. Wang, J. Jing, F. Xu, Z. Li, Q. Wei, P. Cigler, and Z. Chu, Toward quantitative bio-sensing with nitrogen-vacancy center in diamond, *Nat. Commun.* **6**, 2077-2107 (2021).
  - [12] P. Neumann, I. Jakobi, F. Dolde, C. Burk, R. Reuter, G. Waldherr, J. Honert, T. Wolf, A. Brunner, J. H. Shim, D. Suter, H. Sumiya, J. Isoya, and J. Wrachtrup, High-precision nanoscale temperature sensing using single defects in diamond, *Nano Lett.* **13**, 2738-2742 (2013).
  - [13] A. Laraoui, H. Aycock-Rizzo, Y. Gao, X. Lu, E. Riedo, and C. A. Meriles, Imaging thermal conductivity with nanoscale resolution using a scanning spin probe, *Nat. Commun.* **6** (2015).
  - [14] J. Rovny, Z. Yuan, M. Fitzpatrick, A. I. Abdalla, L. Futamura, C. Fox, M. C. Cambria, S. Kolkowitz, and N. P. de Leon, Nanoscale covariance magnetometry with diamond quantum sensors, *Science* **378**, 1301 (2022).
  - [15] R. Monge, T. Delord, N. V. Proscia, Z. Shotan, H. Jayakumar, J. Henshaw, P. R. Zangara, A. Lozovoi, D. Pagliero, P. D. Esquinazi, T. An, I. Sodemann, V. M. Menon, and C. A. Meriles, Spin dynamics of a solid-state qubit in proximity to a superconductor, *Nano Lett.* **23**, 422-428 (2023).
  - [16] P. Tamarat, T. Gaebel, J. R. Rabeau, M. Khan, A. D. Greentree, H. Wilson, L. C. L. Hollenberg, S. Prawer, P. Hemmer, F. Jelezko, and J. Wrachtrup, Stark shift control of single optical centers in diamond, *Phys. Rev. Lett.* **97**, 083002 (2006).
  - [17] F. Dolde, H. Fedder, M. W. Doherty, T. Nöbauer, F. Rempp, G. Balasubramanian, T. Wolf, F. Reinhard, L. C. L. Hollenberg, F. Jelezko, and J. Wrachtrup,

- Electric-field sensing using single diamond spins, *Nat. Phys.* **7**, 459 (2011).
- [18] L. C. Bassett, F. J. Heremans, C. G. Yale, B. B. Buckley, and D. D. Awschalom, Electrical tuning of single nitrogen-vacancy center optical transitions enhanced by photoinduced fields, *Phys. Rev. Lett.* **107**, 266403 (2011).
- [19] T. Mittiga, S. Hsieh, C. Zu, B. Kobrin, F. Machado, P. Bhattacharyya, N. Z. Rui, A. Jarmola, S. Choi, D. Budker, and N. Y. Yao, Imaging the local charge environment of nitrogen-vacancy centers in diamond, *Phys. Rev. Lett.* **121**, 246402 (2018).
- [20] K. Bian, W. Zheng, X. Zeng, X. Chen, R. Stöhr, A. Denisenko, S. Yang, J. Wrachtrup, and Y. Jiang, Nanoscale electric-field imaging based on a quantum sensor and its charge-state control under ambient condition, *Nat. Commun.* **12** (2021).
- [21] W. Ji, Z. Liu, Y. Guo, Z. Hu, J. Zhou, S. Dai, Y. Chen, P. Yu, M. Wang, K. Xia, F. Shi, Y. Wang, and J. Du, Correlated sensing with a solid-state quantum multisensor system for atomic-scale structural analysis, *Nat. Photon.* **18**, 230–235 (2024).
- [22] T. Delord, R. Monge, and C. A. Meriles, Correlated spectroscopy of electric noise with color center clusters, *Nano Lett.* (in press) (2024).
- [23] J. R. Maze, A. Gali, E. Togan, Y. Chu, A. Trifonov, E. Kaxiras, and M. D. Lukin, Properties of nitrogen-vacancy centers in diamond: the group theoretic approach, *New J. Phys.* **13**, 025025 (2011).
- [24] A. Gali, Ab initio theory of the nitrogen-vacancy center in diamond, *Nanophotonics* **8**, 1907–1943 (2019).
- [25] P. Olivero, F. Bosia, B. A. Fairchild, B. C. Gibson, A. D. Greentree, P. Spizzirri, and S. Praver, Splitting of photoluminescent emission from nitrogen–vacancy centers in diamond induced by ion-damage-induced stress, *New J. Phys.* **15** (2013).
- [26] B. A. McCullian, H. F. H. Cheung, H. Y. Chen, and G. D. Fuchs, Quantifying the spectral diffusion of N–V centers by symmetry, *Phys. Rev. Applied* **18** (2022).
- [27] B. A. McCullian, V. Sharma, H. Y. Chen, J. C. Crossman, E. J. Mueller, and G. D. Fuchs, Coherent acoustic control of defect orbital states in the strong-driving limit, *arXiv arXiv:2403.10989* (2024).
- [28] M. E. Trusheim and D. Englund, Wide-field strain imaging with preferentially aligned nitrogen-vacancy centers in polycrystalline, *New J. Phys.* **18** (2016).
- [29] P. Kehayias, M. J. Turner, R. Trubko, J. M. Schloss, C. A. Hart, M. Wesson, D. R. Glenn, and R. L. Walsworth, Imaging crystal stress in diamond using ensembles of nitrogen-vacancy centers, *Phys. Rev. B* **100**, 174103 (2019).
- [30] R. Budnik, O. Cheshnovsky, O. Slone, and T. Volansky, Direct detection of light dark matter and solar neutrinos via color center production in crystals, *Phys. Lett. B* **782**, 242 (2018).
- [31] S. Rajendran, N. Zobrist, A. O. Sushkov, R. Walsworth, and M. Lukin, A method for directional detection of dark matter using spectroscopy of crystal defects, *Phys. Rev. D* **96** (2017).
- [32] A. R. Kirkpatrick, G. Chen, H. Witkowska, J. Brixey, B. L. Green, M. J. Booth, P. S. Salter, and J. M. Smith, Ab initio study of defect interactions between the negatively charged nitrogen vacancy centre and the carbon self-interstitial in diamond, *Phil. Trans. R. Soc. A* **382**, 0174 (2023).
- [33] R. Ebadi, M. C. Marshall, D. F. Phillips, J. Cremer, T. Zhou, M. Titze, P. Kehayias, M. S. Ziabari, N. Delean, and S. R. *et al.*, Directional detection of dark matter using solid-state quantum sensing, *AVS Quantum Sci.* **4** (2022).
- [34] J.-C. Jaskula, E. Bauch, S. Arroyo-Camejo, M. D. Lukin, S. W. Hell, A. S. Trifonov, and R. L. Walsworth, Super-resolution optical magnetic imaging and spectroscopy using individual electronic spins in diamond, *Opt. Express* **25**, 11048 (2017).
- [35] L. Alaerts, Y. Xiong, S. Griffin, and G. Hautier, A first principles study of the stark shift effect on the zero-phonon line of the NV center in diamond, *arXiv arXiv:2403.07771v1* (2024).
- [36] M. Bockstedte, F. Schütz, T. Garratt, V. Ivády, and A. Gali, Ab initio description of highly correlated states in defects for realizing quantum bits, *npj Quantum Materials* **3**, 31 (2018).
- [37] H. Ma, N. Sheng, M. Govoni, and G. Galli, Quantum embedding theory for strongly correlated states in materials, *Journal of Chemical Theory and Computation* **17**, 2116 (2021).
- [38] C. Bhandari, A. L. Wysocki, S. E. Economou, P. Dev, and K. Park, Multiconfigurational study of the negatively charged nitrogen-vacancy center in diamond, *Phys. Rev. B* **103**, 014115 (2021).
- [39] L. Muechler, D. I. Badrtdinov, A. Hampel, J. Cano, M. Rösner, and C. E. Dreyer, Quantum embedding methods for correlated excited states of point defects: Case studies and challenges, *Phys. Rev. B* **105**, 235104 (2022).
- [40] Y. Chen, T. Jiang, H. Chen, E. Han, A. Alavi, K. Yu, E. Wang, and J. Chen, Multiconfigurational nature of electron correlation within nitrogen vacancy centers in diamond, *Phys. Rev. B* **108**, 045111 (2023).
- [41] A. Gali, Recent advances in the ab initio theory of solid-state defect qubits, *Nanophotonics* **12**, 1 (2023).
- [42] S. Haldar, A. Mitra, M. R. Hermes, and L. Gagliardi, Local excitations of a charged nitrogen vacancy in diamond with multireference density matrix embedding theory, *J. Phys. Chem. Lett.* **14**, 4273 (2023).
- [43] G. Pizzi, V. Vitale, R. Arita, S. Blügel, F. Freimuth, G. Géranton, M. Gibertini, D. Gresch, C. Johnson, and T. Koretsune, *et al.*, Wannier90 as a community code: new features and applications, *Journal of Physics: Condensed Matter* **32**, 165902 (2020).
- [44] I. Souza, N. Marzari, and D. Vanderbilt, Maximally localized Wannier functions for entangled energy bands, *Phys. Rev. B* **65**, 035109 (2001).
- [45] F. Aryasetiawan, M. Imada, A. Georges, G. Kotliar, S. Biermann, and A. I. Lichtenstein, Frequency-dependent local interactions and low-energy effective models from electronic structure calculations, *Phys. Rev. B* **70**, 195104 (2004).
- [46] O. Parcollet, M. Ferrero, T. Ayral, H. Hafermann, I. Krivenko, L. Messio, and P. Seth, TRIQS: a toolbox for research on interacting quantum systems, *Comp. Phys. Comm.* **196**, 398 (2015).
- [47] L. J. Rogers, S. Armstrong, M. J. Sellars, and N. B. Manson, Infrared emission of the NV centre in diamond: Zeeman and uniaxial stress studies, *New J. Phys.* **10** (2008).
- [48] V. M. Acosta, A. Jarmola, E. Bauch, and D. Budker, Optical properties of the nitrogen-vacancy singlet levels in diamond, *Phys. Rev. B* **82**, 201202(R) (2010).



- [49] A. Crisci, F. Baillet, M. Mermoux, G. Bogdan, M. Nesládek, and K. Haenen, Residual strain around grown-in defects in CVD diamond single crystals: A 2D and 3D Raman imaging study, *Phys. Status Solidi A* **208**, 2038 (2011).
- [50] V. M. Acosta, C. Santori, A. Faraon, Z. Huang, K.-M. C. Fu, A. Stacey, D. A. Simpson, K. Ganesan, S. Tomljenovic-Hanic, A. D. Greentree, S. Praver, and R. G. Beausoleil, Dynamic stabilization of the optical resonances of single nitrogen-vacancy centers in diamond, *Phys. Rev. Lett.* **108**, 206401 (2012).
- [51] J. Happacher, D. A. Broadway, J. Bocquel, P. Reiser, A. Jimenez, M. A. Tschudin, L. Thiel, D. Rohner, M. li Grimau Puigibert, B. Shields, J. R. Maze, V. Jacques, and P. Maletinsky, Low-temperature photophysics of single nitrogen-vacancy centers in diamond, *PHys. Rev. Lett.* **128**, 177401 (2022).
- [52] T. Delord, R. Monge, G. I. López-Morales, J. Flick, C. E. Dreyer, and C. A. Meriles, in preparation.
- [53] H. Kurokawa, K. Wakamatsu, S. Nakazato, T. Makino, H. Kato, Y. Sekiguchi, and H. Kosaka, Coherent electric field control of orbital state of a neutral nitrogen-vacancy center, *Nat. Commun.* **15**, 4039 (2024).
- [54] A. Lozovoi, H. Jayakumar, D. Daw, G. Vizelethy, E. Bielejec, M. W. Doherty, J. Flick, and C. A. Meriles, Optical activation and detection of charge transport between individual colour centres in diamond, *Nat. Electron* **4**, 717 (2021).